

Ultrathin, Transferred Layers of Metal Silicide as Faradaic Electrical Interfaces and Biofluid Barriers for Flexible Bioelectronic Implants

Jinghua Li,^{†,‡} Rui Li,[§] Haina Du,[‡] Yishan Zhong,[‡] Yisong Chen,[‡] Kewang Nan,^{||} Sang Min Won,[‡] Jize Zhang,[‡] Yonggang Huang,[⊥] and John A. Rogers^{*,†,‡,§,||,⊥}

[†]Department of Materials Science and Engineering, Northwestern University, Evanston, Illinois 60208, United States

[‡]Frederick Seitz Materials Research Laboratory, Department of Materials Science and Engineering, University of Illinois at Urbana—Champaign, Urbana, Illinois 61801, United States

[§]State Key Laboratory of Structural Analysis for Industrial Equipment, Department of Engineering Mechanics, International Research Center for Computational Mechanics, Dalian University of Technology, Dalian 116024, P.R. China

^{||}Department of Mechanical Science and Engineering, Frederick Seitz Materials Research Laboratory, University of Illinois at Urbana—Champaign, Urbana, Illinois 61801, United States

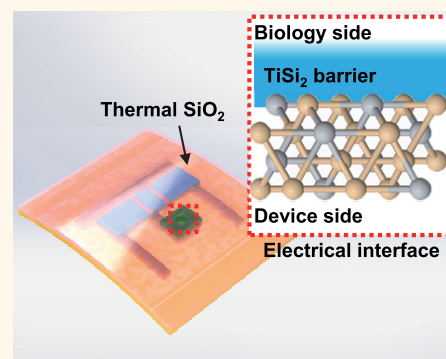
[⊥]Department of Mechanical Engineering, Civil and Environmental Engineering, and Materials Science and Engineering, Northwestern University, Evanston, Illinois 60208, United States

[#]Center for Bio-Integrated Electronics, Departments of Biomedical Engineering, Neurological Surgery, Chemistry, Mechanical Engineering, Electrical Engineering and Computer Science, Simpson Querrey Institute for Nano/biotechnology, Northwestern University, Evanston, Illinois 60208, United States

Supporting Information

ABSTRACT: Actively multiplexed, flexible electronic devices represent the most sophisticated forms of technology for high-speed, high-resolution spatiotemporal mapping of electrophysiological activity on the surfaces of the brain, heart, and other organ systems. Materials that simultaneously serve as long-lived, defect-free biofluid barriers and sensitive measurement interfaces are essential for chronically stable, high-performance operation. Recent work demonstrates that conductively coupled electrical interfaces of this type can be achieved based on the use of highly doped monocrystalline silicon electrical “via” structures embedded in insulating nanomembranes of thermally grown silica. A limitation of this approach is that dissolution of the silicon in biofluids limits the system lifetimes to 1–2 years, projected based on accelerated testing. Here, we introduce a construct that extends this time scale by more than a factor of 20 through the replacement of doped silicon with a metal silicide alloy (TiSi₂). Systematic investigations and reactive diffusion modeling reveal the details associated with the materials science and biofluid stability of this TiSi₂/SiO₂ interface. An integration scheme that exploits ultrathin, electronic microcomponents manipulated by the techniques of transfer printing yields high-performance active systems with excellent characteristics. The results form the foundations for flexible, biocompatible electronic implants with chronic stability and Faradaic biointerfaces, suitable for a broad range of applications in biomedical research and human healthcare.

KEYWORDS: thin-film encapsulation, metal silicide, Faradaic contact, flexible electronics, biofluid barriers



A critical area of research on thin, flexible, implantable electronic systems involves the development of materials and device designs that enable safe, long-term operation in biofluids with little or no degradation in performance.^{1–12} For implants such as cardiac pacemakers and deep brain stimulators, a relevant operational time frame corresponds to the life of the patient. For systems designed with robust engineering margins, the corresponding targeted

lifetimes might approach 100 years or more. A specific class of device of interest here involves ultrathin, mechanically flexible systems that incorporate active silicon electronics in the form of arrays of transistors for multiplexed operation and local

Received: October 12, 2018

Accepted: December 28, 2018

Published: January 4, 2019

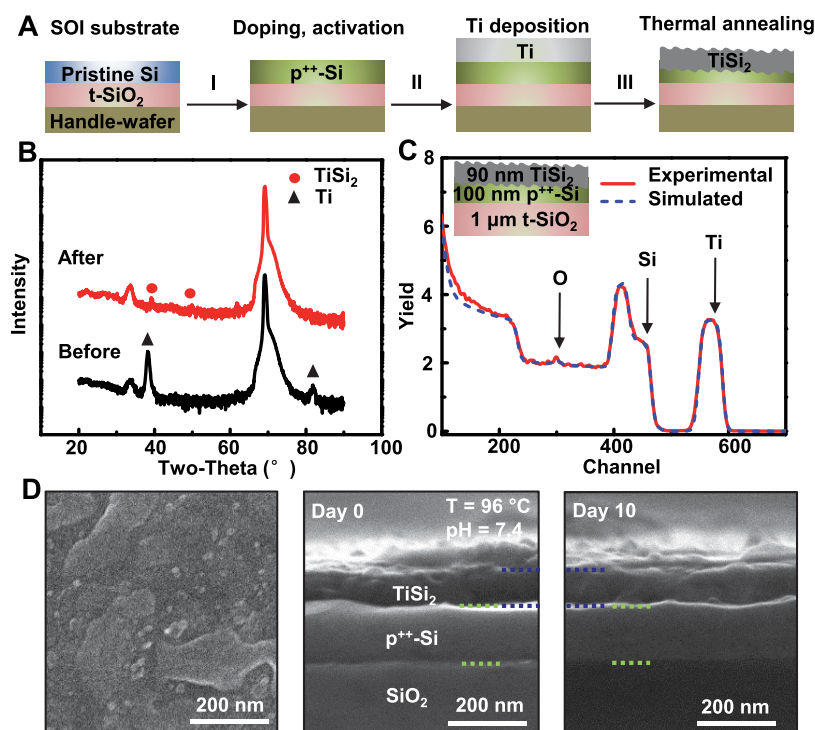


Figure 1. Material preparation and characterization of titanium silicide on silicon-on-insulator (SOI substrate). (A) Steps for forming structures of TiSi_2 and highly p-doped Si bilayer on thermally grown silicon dioxide: (I) doping top-layer pristine Si by thermal diffusion of boron to form $\text{p}^{++}\text{-Si}$ (concentration: 10^{20} atoms/ cm^3); (II) depositing Ti on top of $\text{p}^{++}\text{-Si}$; (III) forming TiSi_2 film by thermal annealing at 850°C in Ar. (B) X-ray diffraction patterns of SOI substrate with Ti before (black) and after (red) thermal annealing, confirming the formation of TiSi_2 in orthorhombic structure. (C) Rutherford backscattering spectra of TiSi_2 film formed with 40 nm Ti on 180 nm $\text{p}^{++}\text{-Si}$. The measured thickness after thermal annealing (90 nm for TiSi_2 and 100 nm for $\text{p}^{++}\text{-Si}$) indicates Ti reacts with Si in a 1:2 ratio. (D) Scanning electron microscopy images of surface morphology of TiSi_2 (left), with side views showing no change in the thickness of ~ 90 nm TiSi_2 as a result of soaking in PBS (pH 7.4) at 96°C for 10 days (middle and right).

signal amplification, with capabilities in high-speed, high-resolution, large-area mapping of electrophysiological activity across the curved, dynamic surfaces of the brain, heart, or other organs.^{10,13–22} The development of interface materials that can serve as chronically stable barriers to isolate the backplane electronics in these systems from the adjacent biotissues and biofluids represents a daunting challenge.^{23–26} Ideally, these interface materials should also provide direct conductive coupling and capabilities for Faradaic charge injection, as the basis for optimal measurement fidelity and, in the case of stimulation, charge transfer.²⁷ For capacitive interfaces, ultrathin, physically transferred layers of thermal SiO_2 (t-SiO_2) exhibit exceptional characteristics, as defect-free, mechanically flexible materials that can serve as barriers with projected lifetimes of several decades in simulated biofluids. Recent reports show that incorporating patterned regions of highly doped silicon into the t-SiO_2 yields electrical “via” structures (denoted as $\text{p}^{++}\text{-Si}/\text{t-SiO}_2$) to conductive pads on the opposite side that serves as conductive biointerfaces.²⁸

Although this approach yields a stable platform for flexible electronic systems, the rate of dissolution of the silicon under physiological conditions (0.5–100 nm/day depending on ionic concentrations and other factors)²⁹ is orders of magnitude higher than that of t-SiO_2 (0.04–1.26 nm/day).^{14,30} As a result, dissolution of the silicon limits the lifetimes of electronic platforms with 100 nm thick layers of Si nanomembranes as encapsulation to values in the range of 0.5–2 years. The ideal solution to this problem would provide a thin and conductive

water barrier that does not react with biofluids for chronic and high-quality bioimplants.

The results reported here show that replacing the silicon with a bilayer structure of a metal silicide alloy and silicon enhances the operating lifetimes of these types of implantable electronic systems by more than an order of magnitude. Specifically, TiSi_2 , formed by the high-temperature reaction of thin metal films of titanium deposited on monocrystalline silicon, represents an attractive choice due to the biocompatibility and low cost of Ti and the high conductivity of the alloy.³¹ When generated from the device layer of silicon on a silicon-on-insulator (SOI) wafer, the TiSi_2 intimately bonds to the t-SiO_2 that serves as the buried oxide to yield a construct denoted as $\text{p}^{++}\text{-Si}/\text{TiSi}_2//\text{t-SiO}_2$. Here, the use of “/” indicates an interface between films, and “//” indicates a *via* structure through another layer. An aligned opening formed through the underside of the t-SiO_2 after removal of the supporting wafer yields a Faradaic contact interface between adjacent biological tissues and electronics on the opposite side. Flexible systems built with ultrathin silicon transistors integrated by transfer printing onto the surface of the t-SiO_2 exhibit long-lived, high-performance operation when immersed in biofluids, limited only by the spatial uniform, slow dissolution of the t-SiO_2 . Detailed studies, including temperature-dependent soak tests, reactive diffusion modeling, leakage measurements, and electrical performance assessments reveal the material properties and key advantages of TiSi_2 in this context. Demonstrations with basic electronic components including passive electrodes and metal-oxide-semiconductor field-effect transis-

tors (MOSFETs) highlight the essential features of the approach. This metal silicide alloy thin film serves as an excellent electrical interface and encapsulation for various flexible electronic systems at the micro- and nanoscale for electrophysiological sensing and electrical stimulation, with high fidelity operation.

RESULTS AND DISCUSSION

Figure 1A presents a schematic illustration of steps for preparing the TiSi_2 . Here, $\text{p}^{++}\text{-Si}$, TiSi_2 , and t-SiO_2 are derived from a monocrystalline Si nanomembrane. Doping and silicidation take place on a silicon-on-insulator substrate purchased from University Wafer, as described in Figure 1A. The sequence begins with an SOI substrate (Figure 1A,I). Thermal diffusion with a boron solid source at 1000 °C for 15 min yields $\text{p}^{++}\text{-Si}$ from the device layer of silicon on the top of the SOI with a carrier concentration of $10^{20}/\text{cm}^3$ (Figure 1A,II, initial concentration: $10^{17}/\text{cm}^3$). Electron-beam evaporation and photolithography forms patterned pads of thin Ti on the $\text{p}^{++}\text{-Si}$. Thermal annealing at 850 °C creates TiSi_2 , with some remaining $\text{p}^{++}\text{-Si}$ underneath. An important aspect of this step is that it only partially consumes the $\text{p}^{++}\text{-Si}$ to yield a rough interface between the Si and the TiSi_2 , thus avoiding through-thickness and interfacial defects that could otherwise result from the large volumetric increases associated with the silicidation. Figure S1 presents images of TiSi_2 with defects caused by the silicidation with excess amounts of Ti. The thickness of the Ti defines the ratio of TiSi_2 to $\text{p}^{++}\text{-Si}$. This ratio balances considerations for creating a layer of TiSi_2 sufficiently thick to act as an effective barrier to secure 100% yield of long lifetime operation but sufficiently thin to leave a continuous layer of $\text{p}^{++}\text{-Si}$ after silicidation, including its rough interface to the TiSi_2 (previous studies report the interface root-mean-square roughness for TiSi_2 formed at 890 °C to be 22 nm).³² In most cases reported here, the ratio of thicknesses (TiSi_2 to $\text{p}^{++}\text{-Si}$) is $\sim 1:1$, as will be discussed below.

X-ray diffraction patterns collected before (black) and after (red) silicidation yield additional information associated with this process (Figure 1B). Peaks associated with crystalline, highly oriented (001) Ti (black triangles) with hexagonal structure disappear after annealing, and the sample shows peaks corresponding to low resistivity phase C54- TiSi_2 (red dots).³³ The sheet resistance drops from ~ 50 to $\sim 2.5 \Omega/\text{sq}$ after annealing, consistent with the high conductivity of the alloy. These results confirm the complete reaction of Ti and the formation of TiSi_2 in the orthorhombic structure. Studies using 2 MeV 4He^+ Rutherford backscattering spectroscopy (RBS) provide the depth-dependent elemental content of the multilayer structure formed by the reaction between 40 nm Ti and 180 nm $\text{p}^{++}\text{-Si}$ (Figure 1C). The dashed curve corresponds to simulations of the backscattering spectrum of the target sample for RBS analysis, obtained using the software SIMNRA 7.0. The simulated and experimental curves fit closely, suggesting good accuracy for the measured thicknesses of TiSi_2 , $\text{p}^{++}\text{-Si}$, and t-SiO_2 . The data show 90 nm of TiSi_2 and 100 nm of $\text{p}^{++}\text{-Si}$, consistent with the expected reaction of Ti with Si in a 1:2 ratio. Scanning electron microscopy (SEM) images in Figure 1D highlight the surface morphology (left) and the cross-sectional profile (middle and right) of the sample after thermal annealing. Immersing the substrate with the TiSi_2 on the top into phosphate-buffered saline (PBS) (Figure 1D) allows for measurements of the reactive dissolution of this material. Unlike the previously reported case of $\text{p}^{++}\text{-Si}/\text{t-SiO}_2$,

where significant reductions in the thickness of the electrical interface material (*i.e.*, Si) occur due to immersion in PBS,^{14,28–30} the TiSi_2 exhibits no measurable change, even for soaking in PBS at 96 °C for 10 days (pH 7.4). This observation suggests that the TiSi_2 is completely insoluble, from a practical standpoint, and that the lifetime of the resulting interface construct is limited only by dissolution of the t-SiO_2 . Although the current studies use PBS as a substitute for biofluids, other components and interactions may also alter some of the conclusions here, such as nonspecific interactions of proteins.

A schematic illustration of the overall structure and the integration strategy for conductively coupled flexible platforms with the $\text{p}^{++}\text{-Si}/\text{TiSi}_2/\text{t-SiO}_2$ as a Faradaic electrical interface appears in Figure 2. Doping, deposition, patterning, and

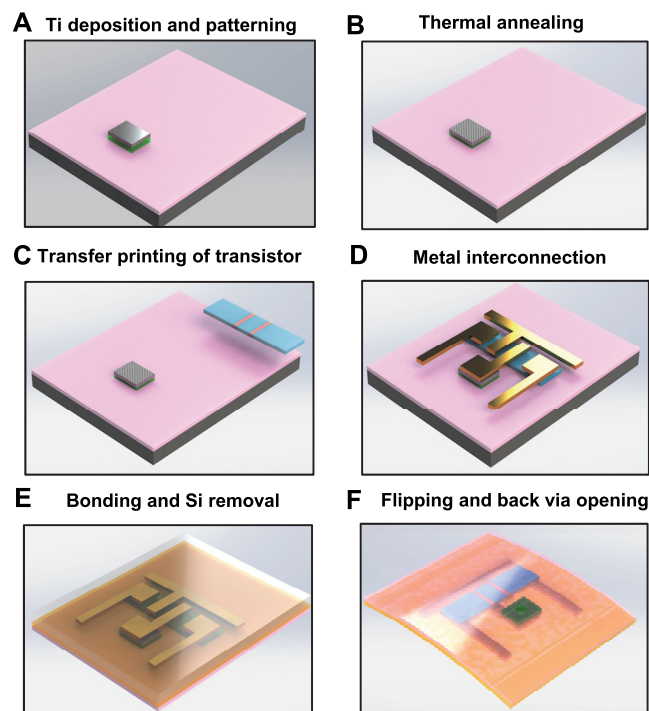


Figure 2. Schematic illustration of the fabrication and integration steps for using monolithically bonded structures of TiSi_2 , $\text{p}^{++}\text{-Si}$, and thermally grown silicon dioxide as electrical biointerfaces and biofluid barriers in a flexible, biointegrated electronic system. (A) Doping, depositing, and patterning regions of $\text{p}^{++}\text{-Si}$ and Ti on a SOI substrate. (B) Thermal annealing to form TiSi_2 and $\text{p}^{++}\text{-Si}$ as described in Figure 1A. (C) Placing a transistor next to TiSi_2 using transfer printing. (D) Fabricating active circuits containing MOSFET and TiSi_2 . (E) Bonding the circuits to a glass substrate coated with polyimide thin film (12 μm) and removing the handle Si by reactive ion etching. (F) Flipping the device, forming *via* openings through the SiO_2 , and peeling the device away from the glass substrate.

etching steps form isolated islands of $\text{p}^{++}\text{-Si}$ and Ti on SOI substrates (Figure 2A). Thermal annealing yields TiSi_2 (Figure 2B). Transfer printing places a collection of separately fabricated, n-type transistors based on nanomembranes of monocrystalline silicon (Si NMs) at locations adjacent to the pads of TiSi_2 (Figure 2C). The fabrication of the transistors begins with device-grade Si NMs derived from SOI wafers, as purchased (p-type Si, concentration: 10^{17} atom/ cm^3). The subsequent steps follow standard procedures for forming n-

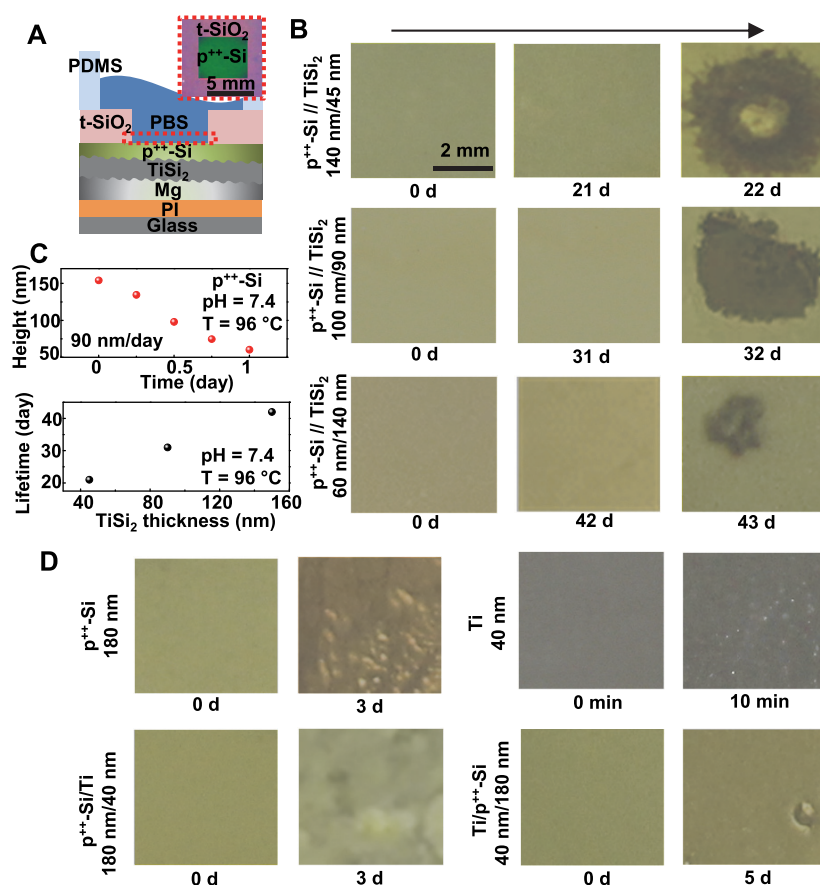


Figure 3. Effect of the encapsulation layer thickness and materials type on the lifetime of devices. (A) Schematic illustration of the device structure for tests that use a thin film of Mg as a sensor for water penetration (inset: top view showing the exposed p⁺⁺-Si//TiSi₂ barrier layer). (B) Sequence of optical images of Mg in a representative test device immersed in PBS solution (pH 7.4) at 96 °C with different thickness of p⁺⁺-Si and TiSi₂. (C) Change in thickness of a membrane of p⁺⁺-Si as a function of immersion time in PBS at 96 °C and summary of lifetime of a p⁺⁺-Si//TiSi₂ barrier with different thickness, as shown in Figure 3B. (D) Results of accelerated immersion tests using different barrier materials.

type MOSFETs. We used transfer-printed transistors in the following studies of active circuits that contain MOSFET and TiSi₂. Subsequent deposition, lithography, and etching steps yield interconnections between these transistors and p⁺⁺-Si/TiSi₂ as the Faradaic biointerface (Figure 2D). A transfer process bonds the top of the structure to a temporary glass substrate that supports a thin film of polyimide (PI). Eliminating the silicon substrate leaves the bottom side of the buried t-SiO₂ exposed (Figure 2E). Flipping the structure and removing the t-SiO₂ at small regions centered at the locations of the pads of p⁺⁺-Si/TiSi₂ exposes the conductive interface. As an option, metal pads can be formed in patterned arrays aligned to these openings as a means to increase the fill factor of the conductive interface, in a manner similar to that described previously.²⁸ Peeling the device away from the glass completes the process (Figure 2F). In this design, the monolithic structure of t-SiO₂, p⁺⁺-Si, and TiSi₂ together acts as the barrier against biofluid penetration. The conductive p⁺⁺-Si/TiSi₂ bilayer enables Faradaic contact with biotissues *via* an electrical interface to the channel of the transistor. The fabrication process flips the sequence of materials layers as described in Figure 1. In the following study, the soak tests involve the structure biofluid/ p⁺⁺-Si/TiSi₂// t-SiO₂.

Soak tests using structures of p⁺⁺-Si/TiSi₂//t-SiO₂ formed in this way, but with thin layers of magnesium in place of the electronics (described subsequently), enable rapid, visual

evaluation of water penetration that follows from hydrolysis of the magnesium ($\text{Mg} + 2\text{H}_2\text{O} = \text{Mg}(\text{OH})_2 + \text{H}_2$). The Mg serves as a visual means to detect the penetration of water, as it only reacts with water if the encapsulation layer fails and allows water to pass. Its presence does not affect the processes of dissolution before the point of failure. Other materials that react rapidly with water, such as calcium, could also be used for similar purposes. Due to the slow dissolution rate of p⁺⁺-Si and t-SiO₂, PBS solution at elevated temperature serves as a means to evaluate the lifetime and to study the chemical and physical processes. Accelerated immersion tests correspond to studies of dissolution processes at elevated temperatures. The aim is to increase the rates of dissolution, to allow assessments of reaction rates on laboratory time scales that are too small at room or body temperatures. From measurements at multiple temperatures, Arrhenius scaling laws can be applied to extrapolate lifetimes at elevated temperatures to those at body temperature.^{14,28,34}

A schematic illustration of the experimental setup appears in Figure 3A (inset is a photograph of the top view of the test structure). Here, a 5 × 5 mm² opening through the t-SiO₂ exposes p⁺⁺-Si/TiSi₂ to surrounding PBS solution (pH 7.4) confined in a well built with poly(dimethylsiloxane) (PDMS; Sylgard 184, Dow Corning). A thin film of Mg under the encapsulation layer serves as a sensor to detect water penetration. Figure 3B shows a sequence of optical images of

Mg encapsulated by p^{++} -Si/TiSi₂ with different thickness combinations during soak tests in PBS at 96 °C. The bilayer of 140 nm p^{++} -Si and 45 nm TiSi₂ provides stable encapsulation for 21 days, at which point the Mg dissolves quickly and uniformly. Additional studies on the same test system reveal lifetimes of 15 days at 100 °C. Immersion at 37 °C provides additional information on the chronic stability. The devices have survived for 0.5 years under these conditions and remain intact as of the writing of this article. Similar experiments with different thickness combinations of p^{++} -Si/TiSi₂ (100/90 nm and 60/140 nm) reveal lifetimes of 31 and 42 days, respectively, at 96 °C. Separate evaluations using reflectometry (MProbe, Semicon Soft) show that the rate of dissolution of p^{++} -Si in PBS at 96 °C is ~ 90 nm/day (Figure 3C, top). In this sense, the p^{++} -Si is transient and dissolves within 1–2 days at 96 °C. The remaining TiSi₂/t-SiO₂ structure serves as the biofluid barrier and conductive biointerface, with long lifetimes due to the relative insolubility of the TiSi₂.

The biocompatibility of the products of dissolution of p^{++} -Si, specifically those associated with the dopants, merits some attention. Previous studies established the biocompatibility of doped silicon with low to moderate doping levels.^{35,36} The total mass content of boron is extremely low in our ultrathin layers of p^{++} -Si even at a doping concentration of 10^{20} atom/cm³. Specifically, the amount of boron in a uniform sheet of p^{++} -Si (5×5 cm², 100 nm thick) is ~ 400 ng. A point of comparison is the average adult dietary intake, which is ~ 1 mg/day, and the tolerable upper intake level for adults, which is 20 mg/day.³⁷ Ongoing efforts seek to further investigate the effect of highly doped Si NM on biotissues for their applications in bioelectronics implants.

Figure 3C (bottom) summarizes the correlations between the thickness of the TiSi₂ and the lifetime. In all three cases, the dissolution of Mg initiates at a single point and then propagates laterally across the entire surface. Secondary ion mass spectrometry reveals more details about the failure mechanism. Figure S2 in the Supporting Information shows the cross-sectional depth profile of [Na⁺] in a layer of TiSi₂ with a thickness of 90 nm on a SOI substrate and immersed in PBS (pH 7.4) at increased temperature (96 °C). The concentration of Na⁺ increases by ~ 10 times after 10 days and ~ 1000 times after 30 days, suggesting the gradual diffusion of PBS through point defects related, for example, to vacancies or interstitial depletion, as reported in previous studies of this material.³² Figure 3D summarizes results for other encapsulation structures. A 170 nm thick layer of p^{++} -Si survives for only 2 days, consistent with the dissolution rate of p^{++} -Si mentioned in Figure 3C. A single layer of Ti (40 nm) formed by electron-beam evaporation leads to almost immediate failure (~ 10 min) even at room temperature due to the penetration of water through pinholes and/or grain boundaries. Similarly, adding a layer of Ti between p^{++} -Si and Mg without silicidation does not improve the lifetime compared to p^{++} -Si alone (2 days). Coating Ti onto the side of p^{++} -Si in contact with PBS increases the lifetime compared to bare p^{++} -Si by a factor of ~ 2 , mainly by slowing the rate of diffusion of water to the surface of the silicon.

Figure 4 shows the results of theoretical modeling of reactive diffusion for dissolution of Mg with TiSi₂ encapsulation. The schematic illustration of the model appears in Figure 4A, where a one-dimensional geometry is sufficient because the initial thickness (in the z direction) is much smaller than the lateral dimensions (in the directions perpendicular to the z axis).

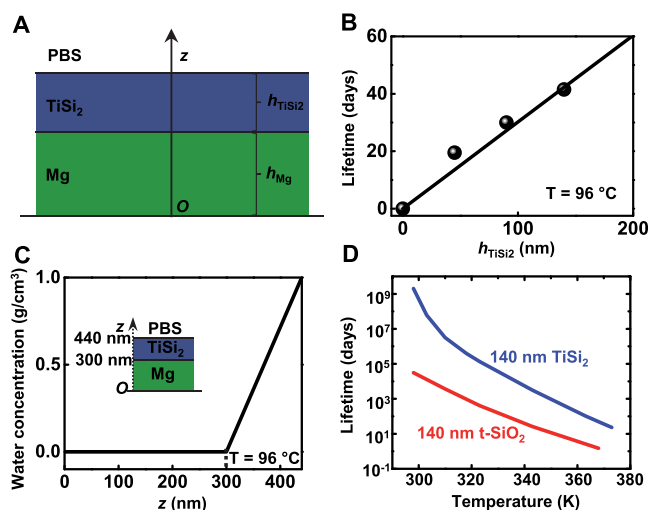


Figure 4. Theoretical modeling of reactive diffusion for dissolution of Mg with TiSi₂ encapsulation. (A) Schematic illustration of the model. (B) Theoretical (line) and measured (dots) lifetimes of a Mg/TiSi₂ structure with a constant 300 nm thick Mg layer and different thicknesses of TiSi₂ layers. (C) Distribution of saturated water concentration in a 300/140 nm thick Mg/TiSi₂ bilayer (inset: a schematic illustration of the geometry). (D) Theoretical prediction of temperature-dependent lifetimes of 300/140 nm thick Mg/TiSi₂ and Mg/t-SiO₂ bilayers.

Because TiSi₂ does not react with water, as suggested by experimental observations, the model only involves the diffusion through TiSi₂. The simulations incorporate both reaction and diffusion for Mg due to the rapid hydrolysis ($\text{Mg} + 2\text{H}_2\text{O} \rightarrow \text{Mg}(\text{OH})_2 + \text{H}_2$). This bilayer model describes the transient behavior of the structure, with the origin located at the bottom and the z axis pointing upward (Figure 4A).

The diffusion equation for water in TiSi₂ is $D_{\text{TiSi}_2} \partial^2 w / \partial z^2 = \partial w / \partial t$ ($h_0 \leq z \leq h_0 + h_{\text{TiSi}_2}$), where w is the water concentration, which depends on position z and time t , D_{TiSi_2} is the water diffusivity, and h_0 and h_{TiSi_2} are the initial thicknesses of Mg and TiSi₂ layers, respectively. The reactive diffusion equation³⁸ applies for Mg, that is, $D_{\text{Mg}} \partial^2 w / \partial z^2 - k_{\text{Mg}} w = \partial w / \partial t$ ($0 \leq z \leq h_0$), where D_{Mg} and k_{Mg} are the water diffusivity in Mg and the reaction rate constant between water and Mg, respectively. Here, the reaction follows first-order kinetics.^{39,40} The boundary conditions include $w|_{z=h_0+h_{\text{TiSi}_2}} = w_0$ and $\partial w / \partial z|_{z=0} = 0$, which imply a constant water concentration w_0 ($= 1 \text{ g cm}^{-3}$) at the top surface of the TiSi₂ layer and zero water flux at the bottom surface of the Mg layer. The continuity of both the concentration and the flux of water at the Mg/TiSi₂ interface requires $w|_{z=h_0-0} = w|_{z=h_0+0}$ and $D_{\text{Mg}} \partial w / \partial z|_{z=h_0-0} = D_{\text{TiSi}_2} \partial w / \partial z|_{z=h_0+0}$. Zero water concentration in the structure at $t = 0$ constitutes the initial condition $w|_{t=0} = 0$ ($0 \leq z \leq h_0 + h_{\text{TiSi}_2}$).

Applying the method of separation of variables to the above governing equations under the boundary, continuity, and initial conditions provides an analytic solution of water concentration distributed in the bilayer, which gives the time dependence of the thickness of the Mg layer, h_{Mg} (see details in Methods). The present study applies a simplified expression of h_{Mg} , $h_{\text{Mg}}/h_0 \approx 1 - t/t_{\text{critical}}$, where

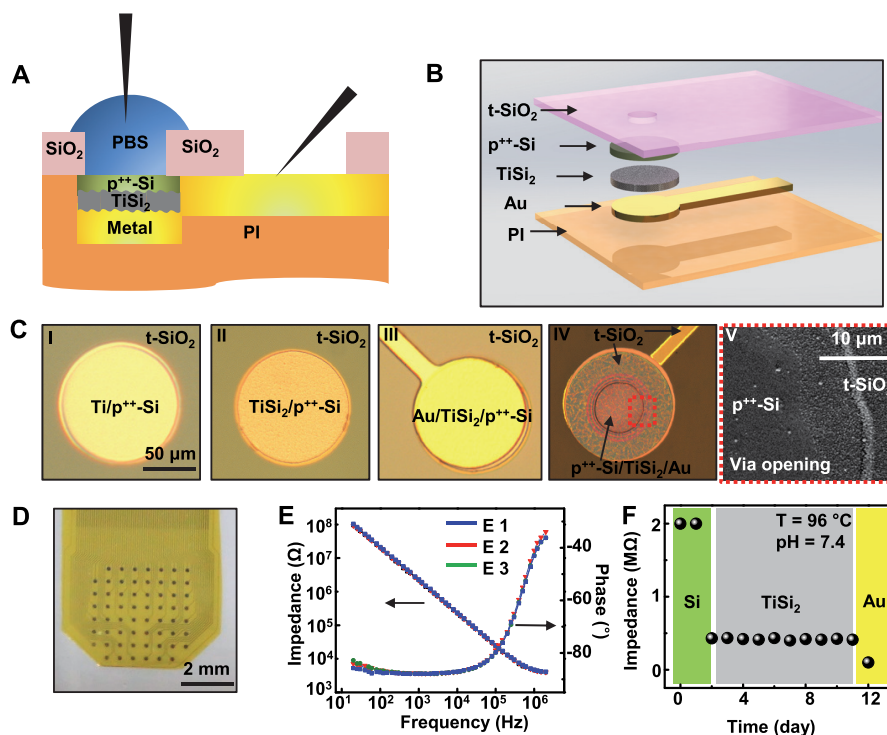


Figure 5. Demonstration of thin and flexible passive electrode arrays encapsulated with p^{++} -Si and $TiSi_2$. Schematic cross-sectional (A) and exploded-view (B) illustrations of a passive electrode for electrophysiology. (C) Optical images of the fabrication sequence. (I) Ti deposition on silicon; (II) thermal annealing for silicide formation; (III) Au deposition to form metal interconnects; (IV) handle-wafer removal and back *via* opening (diameter: $50\ \mu\text{m}$); (V) SEM image highlighting the step edge between the $t\text{-SiO}_2$ and the p^{++} -Si in the *via* opening. (D) Photograph of a 61-channel passive electrode system in flexible form. (E) Electrochemical impedance spectra of passive electrodes at three different recording sites showing uniform magnitude and phase responses. (F) Time evolution of device impedance at 1 kHz associated with different constituent materials during the dissolution test. Days 0–1: device encapsulated with p^{++} -Si. Days 2–11: device encapsulated with $TiSi_2$. Day 12: Au interconnects exposed to PBS due to $t\text{-SiO}_2$ dissolution.

$$t_{\text{critical}} = \frac{qh_0\rho_{\text{Mg}}M_{\text{H}_2\text{O}}}{w_0M_{\text{Mg}}\sqrt{k_{\text{Mg}}D_{\text{Mg}}}\tanh\sqrt{\frac{k_{\text{Mg}}h_0^2}{D_{\text{Mg}}}} \times \left(1 + \frac{h_{\text{TiSi}_2}}{D_{\text{TiSi}_2}}\sqrt{k_{\text{Mg}}D_{\text{Mg}}}\tanh\sqrt{\frac{k_{\text{Mg}}h_0^2}{D_{\text{Mg}}}}\right) \quad (1)$$

represents the lifetime of the bilayer structure, that is, the time when the Mg layer fully dissolves ($h_{\text{Mg}} = 0$). Herein, q ($=2$) is the number of water molecules that react with each atom of Mg, ρ_{Mg} ($=1.74\ \text{g cm}^{-3}$) is the mass density of Mg, and $M_{\text{H}_2\text{O}}$ ($=18\ \text{g mol}^{-1}$) and M_{Mg} ($=24\ \text{g mol}^{-1}$) are the molar masses of water and Mg, respectively. Both single-layer and bilayer reactive diffusion models determine the key parameters, k_{Mg} , D_{Mg} , and D_{TiSi_2} ,⁴¹ based on the soak tests (see details in Methods). For example, $k_{\text{Mg}} = 26.8\ \text{s}^{-1}$, $D_{\text{Mg}} = 1.9 \times 10^{-10}\ \text{cm}^2\ \text{s}^{-1}$, and $D_{\text{TiSi}_2} = 3 \times 10^{-16}\ \text{cm}^2\ \text{s}^{-1}$ in PBS solution at $96\ ^\circ\text{C}$. Arrhenius scaling provides the constants at other temperatures (see Methods).

Figure 4B shows the change in lifetime the Mg/ $TiSi_2$ bilayer with thickness of $TiSi_2$ in PBS solution at $96\ ^\circ\text{C}$, where the initial thickness of Mg is 300 nm. As indicated by eq 1, theoretical modeling reveals an approximately linear dependence of the lifetime on $TiSi_2$ thickness (line), which shows good agreement with the experimental measurements (dots). The distribution of saturated water concentration in a 300/140 nm thick Mg/ $TiSi_2$ bilayer before physical disappearance of

Mg appears in Figure 4C, which corresponds to the steady-state limit:

$$\frac{w}{w_0}(z, t \rightarrow \infty) = \begin{cases} \frac{\cosh\left(\sqrt{\frac{k_{\text{Mg}}}{D_{\text{Mg}}}}z\right)}{\cosh\sqrt{\frac{k_{\text{Mg}}h_0^2}{D_{\text{Mg}}}} + \sqrt{k_{\text{Mg}}D_{\text{Mg}}}\frac{h_{\text{TiSi}_2}}{D_{\text{TiSi}_2}}\sinh\sqrt{\frac{k_{\text{Mg}}h_0^2}{D_{\text{Mg}}}}}, & 0 \leq z \leq h_0 \\ 1 - \frac{h_0 + h_{\text{TiSi}_2} - z}{h_{\text{TiSi}_2} + \frac{D_{\text{TiSi}_2}}{\sqrt{k_{\text{Mg}}D_{\text{Mg}}}}\coth\sqrt{\frac{k_{\text{Mg}}h_0^2}{D_{\text{Mg}}}}}, & h_0 \leq z \leq h_0 + h_{\text{TiSi}_2} \end{cases} \quad (2)$$

Notably, the water concentration dramatically decreases from top to bottom of the $TiSi_2$ layer, reaching a very low level in Mg. This result indicates that the $TiSi_2$ effectively slows the rate of hydrolysis of the underlying Mg. With k_{Mg} , D_{Mg} , and D_{TiSi_2} at different temperatures, the theoretical temperature-dependent lifetime of a 300/140 nm thick Mg/ $TiSi_2$ bilayer appears in Figure 4D (blue line). The lifetime prediction of a Mg/ $t\text{-SiO}_2$ bilayer with the same thicknesses serves as a comparison (red line; see Methods). The results in Figure 4D suggest that the theoretically projected lifetime of $TiSi_2$ at $37\ ^\circ\text{C}$ is 3 orders of magnitude higher than that of a $t\text{-SiO}_2$

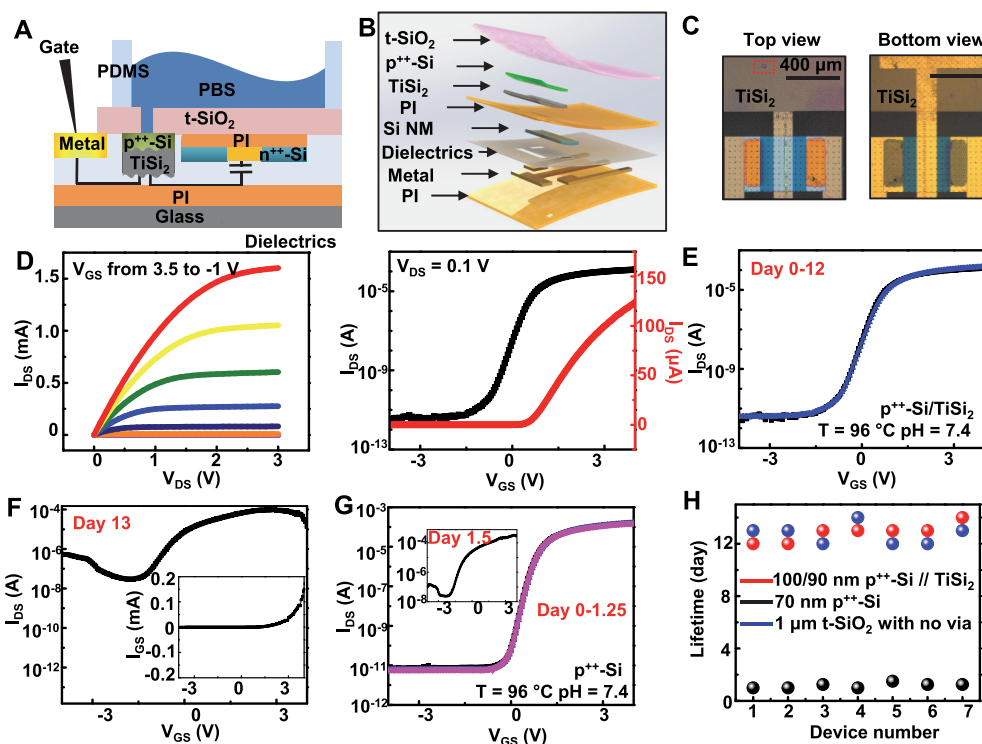


Figure 6. Results for the behavior of NMOS transistors encapsulated with $p^{++}\text{-Si//TiSi}_2$ and immersed in PBS solution at pH 7.4 and 96 °C. Schematic cross-sectional (A) and exploded view (B) illustrations of NMOS transistors encapsulated with $p^{++}\text{-Si//TiSi}_2$. (C) Optical images of an NMOS transistor produced by this manner with a 100/90 nm thick bilayer of $p^{++}\text{-Si//TiSi}_2$ as a barrier on the top connected to its gate electrode with a *via* opening on $t\text{-SiO}_2$. (D) Output (left) and transfer (right) characteristics of a test transistor fabricated in this manner (channel length $L = 20\ \mu\text{m}$, channel width $W = 400\ \mu\text{m}$). (E,F) Results (subthreshold and leakage characteristics) from soak tests of a device with a $p^{++}\text{-Si//TiSi}_2$ *via* exposed to PBS solution at 96 °C. Tests indicate stable operation until failure due to dissolution of the $t\text{-SiO}_2$ after 12 days. (G) Results from soak tests of a device with a $p^{++}\text{-Si}$ ($\sim 70\ \text{nm}$) *via* exposed to PBS solution at 96 °C. Tests indicate stable operation until failure due to dissolution of the $p^{++}\text{-Si}$ after 1.25 days. (H) Summary of lifetimes of seven test devices with $p^{++}\text{-Si//TiSi}_2$ *via*, $p^{++}\text{-Si}$ *via*, and no *via*.

encapsulation with similar thickness (0.04–1.26 nm/day under physiological conditions) based on experimental projections that use the rates of hydrolysis of $t\text{-SiO}_2$.¹⁴

Figure 5 demonstrates the use of TiSi_2 as both an electrical interface for Faradaic contact and a barrier layer in a flexible platform of individually addressed passive electrodes. Here, the thicknesses of the $p^{++}\text{-Si}$, TiSi_2 , and $t\text{-SiO}_2$ are 100 nm, 90 nm, and 1 μm , respectively. Figure 5A,B shows the cross-sectional and exploded schematic illustrations of the device structure, respectively. Openings (diameter: 50 μm) through the $t\text{-SiO}_2$ define areas of $p^{++}\text{-Si//TiSi}_2$ that electrically connect to gold electrodes. A flexible film of PI serves as the substrate. Optical microscope and scanning electron microscope images in Figure 5C highlight the structure of the device after key fabrication steps (I–IV) as well as the step edge between $t\text{-SiO}_2$ and $p^{++}\text{-Si}$ (V). A photograph of a 61-channel system is shown in Figure 5D. Electrochemical impedance spectra measured in PBS solution at room temperature provide additional information. Figure 5E shows the magnitude of the impedance and the phase angle of electrodes collected at three different recording sites. The results indicate high uniformity in response. The impedance at 1 kHz (the frequency most relevant to neural sensing) is $\sim 2\ \text{M}\Omega$. The coating and patterning of conductive materials (e.g., Pt, Au, and conductive polymers) aligned to these openings can further slow the diffusion of water as well as reduce the interfacial impedance for applications in high-resolution electrophysiological recordings. The three-stage time evolution of a representative electrode during a soak

test in PBS at 96 °C appears in Figure 5F. The impedance drops abruptly at day 3, suggesting the complete dissolution of $p^{++}\text{-Si}$ and the exposure of highly conducting TiSi_2 . Another significant decrease in impedance occurs at day 12, corresponding to the dissolution of $t\text{-SiO}_2$ and a corresponding increase in contact area of the electrode with PBS. The lateral dimensions of the $p^{++}\text{-Si}$ layer and the size/density of the openings in the $t\text{-SiO}_2$ can be important factors in determining the lateral diffusion of biofluids that could limit the lifetime of the electronics. Specifically, for certain combinations of dimensions, it is possible for the $p^{++}\text{-Si}$ to dissolve laterally ($\sim 0.5\ \text{nm/day}$ at 37 °C, Figure S3) while the TiSi_2 is still intact. Based on this result, the minimum lateral distance required between the edge of the opening to the edge of the $p^{++}\text{-Si}$ can be estimated. For instance, to ensure a targeted lifetime of 50 years at 37 °C, the minimal lateral distance is $\sim 9\ \mu\text{m}$, as determined by 50 years \times 365 day/year \times 0.5 nm/day.

Soak testing of similar devices but with active electronic functionality yields additional information on lifetime and stability. Schematic illustrations of cross-sectional and exploded views are in Figure 6A,B, respectively. Each test device includes an n-type MOSFET (channel length = 20 μm , channel width = 400 μm) transfer printed onto the SOI substrate and connected to the patterned TiSi_2 through the gate electrode (Figure 6C). A *via* opening formed through the $t\text{-SiO}_2$ on the opposite side exposes the $p^{++}\text{-Si//TiSi}_2$ interface to PBS. Figure 6D illustrates the output (left) and transfer (right, linear and log scale) characteristics. The transistors have

mobilities of $\sim 300 \text{ cm}^2 \text{ V}^{-1} \text{ s}^{-1}$, on/off ratios of 10^7 , subthreshold swings of $\sim 200 \text{ mV/dec}$, threshold voltages of 0.7 V , and Ohmic contact behaviors. Mechanical bending tests illustrate the robustness and flexibility of the system (Figure S4). The electrical performance remains stable with a bending radius of $\sim 1 \text{ cm}$ for 500 cycles. In the soak testing at 96°C , the transistor remains functional and stable until day 12 (Figure 6E), after which a sudden increase in leakage current causes catastrophic failure (Figure 6F, inset: leakage current). Considering that the observed lifetime (12 days) is consistent with the complete dissolution of $1 \mu\text{m}$ t-SiO₂ at 96°C as reported in literature, it is reasonable to attribute the failure of the device to the penetration of PBS into the transistor, including the dielectrics. The observation of bubbles in the transistor area supports this hypothesis (Figure S5). We also performed time-dependent dielectric breakdown testing. As shown in Figure S6, the leakage current shows a sudden increase on day 13, indicating that the dielectrics remain stable until complete dissolution of the t-SiO₂. In contrast, a similar device with only p⁺⁺-Si (70 nm) as the conductive interface has a lifetime of just 1.25 days, defined by dissolution of the p⁺⁺-Si. Figure 6G shows statistics of lifetimes of transistors with different encapsulation layers, including t-SiO₂ with p⁺⁺-Si/TiSi₂ *via* (red), t-SiO₂ with no *via* (blue), and t-SiO₂ with 70 nm p⁺⁺-Si *via* (black). Devices with p⁺⁺-Si/TiSi₂ have lifetimes comparable to those encapsulated by t-SiO₂ with no *via* opening, suggesting that the lifetime is limited only by the dissolution of t-SiO₂. Figures S7 and S8 show the statistical distributions with standard deviations and magnified images of the highly stable material sets, respectively. The sheet resistances of 100 nm p⁺⁺-Si and 100 nm TiSi₂ measured by the four-probe method are ~ 50 and $2.5 \Omega/\text{sq}$, respectively. The heating in the *via* structures is, however, negligible due to very small resistances that follow from short path lengths for current flow. Infrared imaging reported in our previous studies in related systems with t-SiO₂ reveals that there is no apparent increase in temperature associated with operation of the device.¹³

CONCLUSION

In summary, the results presented here establish materials and integration strategies for use of ultrathin TiSi₂ simultaneously as an insoluble biofluid barrier and conductive electrical interface between active, flexible electronic systems and targeted biotissues in chronic implants. Systematic investigations highlight the advantages of TiSi₂ compared to related strategies that use highly doped silicon interfaces. For cases reported here, the ultimate lifetimes of platforms that use this encapsulation strategy are not limited by the conductive interface materials but instead by the slow hydrolysis of capping films of thermally grown silica ($\sim 0.04\text{--}1.26 \text{ nm/day}$ at a pH of 7.4 and 37°C).^{13,14,30} This scheme offers applicability across both passively addressed and actively multiplexed electronic platforms with broad relevance to fundamental research and clinical practice. Such flexible systems offer great potential for long-term and high-performance electrophysiology in neuroscience and other areas. Future efforts include work to implement these concepts in actively multiplexed platforms with varied dimension, sensing unit location and interelectrode distance for studies of electrophysiological processes in the brain and the heart.

METHODS

Preparation of TiSi₂ Thin Films. The sequence for forming TiSi₂ began with the back-grinding of the Si handle of p-type SOI substrate (Soitec) to yield a structure with a 200 nm thick device Si layer (initial doping level: $10^{17} \text{ atom/cm}^3$), a $1 \mu\text{m}$ thick buried oxide layer, and a 200 μm thick handle wafer. The back-grinding takes place on the silicon substrate (handle wafer) side of the system and does not affect the top-layer, device-grade Si NM for doping, silicidation, and device integration. Thermal diffusion and activation of boron in the device silicon yielded p⁺⁺-Si with a concentration of $10^{20} \text{ atom/cm}^3$. Electron-beam evaporation (or sputtering), lithography, and etching created a pattern of pads of Ti on p⁺⁺-Si. Thermal annealing at 850°C formed TiSi₂ with some remaining p⁺⁺-Si underneath. Ti reacted with Si in a 1:2 ratio.

Fabrication Methods for Devices and Test Structures with a TiSi₂ Encapsulation Layer. Monocrystalline Si (200 nm) as the device layer on SOI substrates served as the transistor material. A layer of SiO₂ (400 nm) formed by plasma-enhanced chemical vapor deposition (PECVD) served as the diffusion mask. Photolithographic patterning, reactive ion etching (RIE with CF₄/O₂), and wet etching (buffered oxide etchant) followed by thermal diffusion doping with phosphorus at 1000°C defined the source, drain, and channel regions of the transistors. After the removal of the diffusion mask by etching with 49% hydrofluoric acid (HF), another photolithographic step followed by RIE with SF₆ defined regions of *via* holes. The holes enabled etching of the buried oxide layer with 49% HF for 30 min. A flat slab of PDMS (Sylgard 184, 1:4) retrieved the photoresist and Si film for transfer printing onto a thinned SOI substrate (200 μm thick handle wafer) with patterned TiSi₂. A layer of spin-coated polyamic acid (precursor to form PI, 1.5 μm , PI 2545, HD Microsystems) served as the adhesive between the SOI substrate and the transfer-printed Si NMs. Rinsing with acetone removed the photoresist. Baking in a vacuum oven completed the curing process of PI. Photolithography and reaction ion etching with SF₆ patterned the Si film into isolated islands.

PECVD followed by atomic layer deposition (ALD) yielded 50 nm thick layers of SiO₂ and 13 nm thick layers of Al₂O₃, respectively, as a gate dielectric stack. Note that PECVD oxides have higher defects compared to those of thermal oxides and corresponding increases in charge trapping. As a result, the mobility of charge carriers is lower than that of previously reported devices with thermal oxide as the dielectrics.^{14,28} The transistors with PECVD oxides can, nevertheless, offer electrical performance that meets the requirements of the customized data acquisition system for electrophysiological mapping.⁴² Wet etching by BOE formed openings defined by photolithography on the gate stack. Electron-beam evaporation yielded bilayers of 10 nm Cr/300 nm Au as metal contacts. Photolithography and wet etching patterned source, drain, and gate interconnects. Another layer of PI (1.5 μm) encapsulated the metal layer. A coating of 20 nm Al₂O₃ prepared by ALD on the top served as an adhesion layer for bonding to a PI film laminated on a handling glass substrate (with PDMS) and also coated with 20 nm Al₂O₃. Dispensing a commercial adhesive (Kwik-Sil, World Precision Instruments) between the two Al₂O₃-coated layers of PI layers, applying a pressure of $\sim 50 \text{ kPa}$, and curing the adhesive at room temperature for 30 min formed a robust mechanical bond.

RIE with SF₆ and O₂ and inductively coupled plasma RIE (Surface Technology System) removed the handle Si substrate. The highly selective etching of Si exposed t-SiO₂ on the surface. Photolithography and etching with CF₄ and O₂ removed the t-SiO₂ in selected regions above p⁺⁺-Si//TiSi₂. Cutting the device using a razor blade and peeling the device from the substrate completed the fabrication process.

Procedures for the Soak Test. Wells formed with PDMS confined the PBS over the active areas of the devices. Ultraviolet ozone treatment enhanced the adhesion between the t-SiO₂ and PDMS. For the testing of passive electrodes and active transistors, metal traces prepared by electron-beam evaporation, photolithography, and wet etching enabled electrical connections from the central

regions to the probe pads outside of the well. An oven maintained the test devices at stable temperatures.

Theoretical Modeling of Reactive Diffusion. The method of separation of variables was applied to both the diffusion equation for TiSi_2 and reactive diffusion equation for Mg. The analytic solution of water concentration distribution in the bilayer structure was obtained as $w = w_0[\sum_{n=1}^{\infty} C_n \exp(-\lambda_n t) f_n(z) + g(z)]$, with the expressions of C_n , λ_n , and $f_n(z)$ detailed in the Supporting Information. The summation in the above solution shows exponential decay with time, indicating the steady-state limit when $t \rightarrow \infty$, that is, the saturated water concentration, $w = w_0 g(z)$, as given by eq 2, where the right-hand side gives $g(z)$. The time-dependent remaining thickness of the Mg layer was obtained by integrating $k_{\text{Mg}} w M_{\text{Mg}} h_0 / (q \rho_{\text{Mg}} M_{\text{H}_2\text{O}})$ over the thickness direction and time, followed by subtraction from h_0 of the integration. The summation was negligible in the present study (see details in the Supporting Information), which yielded a simplified expression, $h_{\text{Mg}}/h_0 \approx 1 - t/t_{\text{critical}}$, with t_{critical} shown in eq 1.

From a previous study,⁴³ the reaction rate constant k_{Mg} and diffusivity D_{Mg} at 25 and 37 °C were taken; with these known parameters, we determined the two unknowns in the Arrhenius equation describing temperature-dependent k_{Mg} or D_{Mg} which yielded $k_{\text{Mg}} = 10^{(20-6737/T)} \text{ s}^{-1}$ and $D_{\text{Mg}} = 10^{(-3.4-2317/T)} \text{ cm}^2 \text{ s}^{-1}$, where T is the absolute temperature. With the known k_{Mg} and D_{Mg} , the only remaining parameter D_{TiSi_2} at certain temperature could be determined from the present bilayer model by fitting the theoretical lifetime result, as given by eq 1, with that from the experiment. The experimental lifetime results for a 300/90 nm thick Mg/TiSi₂ bilayer were ≈ 30 days at 96 °C and ≈ 15 days at 100 °C, by which we obtained D_{TiSi_2} at the two temperatures. In a similar way to that for k_{Mg} and D_{Mg} , D_{TiSi_2} was determined to be $10^{(9-9058/T)} \text{ cm}^2 \text{ s}^{-1}$ according to Arrhenius scaling. To predict the lifetime of a Mg/t-SiO₂ bilayer (Figure 4D, red line), the constants $k_{\text{t-SiO}_2}$ and $D_{\text{t-SiO}_2}$ were extracted from a previous study.³⁴ For example, $k_{\text{t-SiO}_2} = 2.1 \times 10^{14} \times \exp(-15313/T) \text{ s}^{-1}$, $D_{\text{t-SiO}_2} = 5.3 \times 10^{-20} \text{ cm}^2 \text{ s}^{-1}$ at 37 °C, $9.5 \times 10^{-18} \text{ cm}^2 \text{ s}^{-1}$ at 70 °C, and $1.5 \times 10^{-16} \text{ cm}^2 \text{ s}^{-1}$ at 96 °C.

ASSOCIATED CONTENT

Supporting Information

The Supporting Information is available free of charge on the ACS Publications website at DOI: 10.1021/acsnano.8b07806.

Supplementary notes, optical microscopic image of TiSi₂ with defects caused by the deposition of excess amount of Ti followed by thermal annealing, cross-sectional profile of $[\text{Na}^+]$ in 90 nm thick TiSi₂ formed on SOI substrate and immersed in PBS at 96 °C for different times (0, 10, 30 days), measured by secondary ion mass spectrometry, change in thickness of a membrane of p⁺⁺-Si as a function of immersion time in PBS at 37 °C, results of bending tests of the NMOS transistor with TiSi₂ encapsulation, optical image of a transistor encapsulated by p⁺⁺-Si/TiSi₂//t-SiO₂ failed on day 13 (96 °C) showing bubbles, time-dependent dielectric breakdown testing (96 °C, $V_{\text{GS}} = 1 \text{ V}$) showing a sudden increase in leakage current on day 13, statistics of lifetimes of seven test devices with p⁺⁺-Si/TiSi₂ *via*, p⁺⁺-Si *via*, and no *via*, and SEM images of the conductive interface on day 0 (p⁺⁺-Si) and day 12 (TiSi₂) (96 °C) (PDF)

AUTHOR INFORMATION

Corresponding Author

*E-mail: jrogers@northwestern.edu.

ORCID

John A. Rogers: 0000-0002-2980-3961

Notes

The authors declare no competing financial interest.

ACKNOWLEDGMENTS

This work was supported by Defense Advanced Research Projects Agency, Contract HR0011-14-C-0102, and the Center for Bio-Integrated Electronics. We acknowledge the use of facilities in the Micro and Nanotechnology Laboratory for device fabrication and the Frederick Seitz Materials Research Laboratory for Advanced Science and Technology for device measurement at the University of Illinois at Urbana—Champaign. R.L. acknowledges the support from the Young Elite Scientists Sponsorship Program by CAST (No. 2015QNRC001) and Opening Fund of State Key Laboratory of Nonlinear Mechanics, Chinese Academy of Sciences.

REFERENCES

- (1) Litt, B.; Esteller, R.; Echaz, J.; D'Alessandro, M.; Shor, R.; Henry, T.; Pennell, P.; Epstein, C.; Bakay, R.; Dichter, M.; Vachtsevanos, G. Epileptic Seizures May Begin Hours in Advance of Clinical Onset: A Report of Five Patients. *Neuron* **2001**, *30*, 51–64.
- (2) Whitmer, D.; de Solages, C.; Hill, B.; Yu, H.; Henderson, J. M.; Bronte-Stewart, H. High Frequency Deep Brain Stimulation Attenuates Subthalamic and Cortical Rhythms in Parkinson's Disease. *Front. Hum. Neurosci.* **2012**, *6*, 155.
- (3) Canales, A.; Jia, X. T.; Froriep, U. P.; Koppes, R. A.; Tringides, C. M.; Selvidge, J.; Lu, C.; Hou, C.; Wei, L.; Fink, Y.; Anikeeva, P. Multifunctional Fibers for Simultaneous Optical, Electrical and Chemical Interrogation of Neural Circuits *in vivo*. *Nat. Biotechnol.* **2015**, *33*, 277–284.
- (4) Kim, T. I.; McCall, J. G.; Jung, Y. H.; Huang, X.; Siuda, E. R.; Li, Y. H.; Song, J. Z.; Song, Y. M.; Pao, H. A.; Kim, R. H.; Lu, C. F.; Lee, S. D.; Song, I. S.; Shin, G.; Al-Hasani, R.; Kim, S.; Tan, M. P.; Huang, Y. G.; Omenetto, F. G.; Rogers, J. A.; Bruchas, M. R. Injectable, Cellular-Scale Optoelectronics with Applications for Wireless Optogenetics. *Science* **2013**, *340*, 211–216.
- (5) Montgomery, K. L.; Yeh, A. J.; Ho, J. S.; Tsao, V.; Iyer, S. M.; Grosenick, L.; Ferenczi, E. A.; Tanabe, Y.; Deisseroth, K.; Delp, S. L.; Poon, A. S. Y. Wirelessly Powered, Fully Internal Optogenetics for Brain, Spinal and Peripheral Circuits in Mice. *Nat. Methods* **2015**, *12*, 969–974.
- (6) Jeong, J. W.; McCall, J. G.; Shin, G.; Zhang, Y. H.; Al-Hasani, R.; Kim, M.; Li, S.; Sim, J. Y.; Jang, K. I.; Shi, Y.; Hong, D. Y.; Liu, Y. H.; Schmitz, G. P.; Xia, L.; He, Z. B.; Gamble, P.; Ray, W. Z.; Huang, Y. G.; Bruchas, M. R.; Rogers, J. A. Wireless Optofluidic Systems for Programmable *In Vivo* Pharmacology and Optogenetics. *Cell* **2015**, *162*, 662–674.
- (7) Stacey, W. C.; Litt, B. Technology Insight: Neuroengineering and Epilepsy - Designing Devices for Seizure Control. *Nat. Clin. Pract. Neurol.* **2008**, *4*, 190–201.
- (8) McKhann, G. M.; Schoenfeld-McNeill, J.; Born, D. E.; Haglund, M. M.; Ojemann, G. A. Intraoperative Hippocampal Electro-corticography to Predict the Extent of Hippocampal Resection in Temporal Lobe Epilepsy Surgery. *J. Neurosurg.* **2000**, *93*, 44–52.
- (9) Khodagholy, D.; Gelineas, J. N.; Thesen, T.; Doyle, W.; Devinsky, O.; Malliaras, G. G.; Buzsaki, G. NeuroGrid: Recording Action Potentials from the Surface of the Brain. *Nat. Neurosci.* **2015**, *18*, 310–315.
- (10) Viventi, J.; Kim, D. H.; Vigeland, L.; Frechette, E. S.; Blanco, J. A.; Kim, Y. S.; Avrin, A. E.; Tiruvadi, V. R.; Hwang, S. W.; Vanleer, A. C.; Wulsin, D. F.; Davis, K.; Gelber, C. E.; Palmer, L.; Van der Spiegel, J.; Wu, J.; Xiao, J. L.; Huang, Y. G.; Contreras, D.; Rogers, J. A.; Litt, B. Flexible, Foldable, Actively Multiplexed, High-Density Electrode Array for Mapping Brain Activity *in vivo*. *Nat. Neurosci.* **2011**, *14*, 1599–1605.

- (11) Kim, D. H.; Viventi, J.; Amsden, J. J.; Xiao, J. L.; Vigeland, L.; Kim, Y. S.; Blanco, J. A.; Panilaitis, B.; Frechette, E. S.; Contreras, D.; Kaplan, D. L.; Omenetto, F. G.; Huang, Y. G.; Hwang, K. C.; Zakin, M. R.; Litt, B.; Rogers, J. A. Dissolvable Films of Silk Fibroin for Ultrathin Conformal Bio-integrated Electronics. *Nat. Mater.* **2010**, *9*, 511–517.
- (12) Xu, L. Z.; Gutbrod, S. R.; Bonifas, A. P.; Su, Y. W.; Sulkin, M. S.; Lu, N. S.; Chung, H. J.; Jang, K. I.; Liu, Z. J.; Ying, M.; Lu, C.; Webb, R. C.; Kim, J. S.; Laughner, J. I.; Cheng, H. Y.; Liu, Y. H.; Ameen, A.; Jeong, J. W.; Kim, G. T.; Huang, Y. G.; Efimov, I. R.; Rogers, J. A. 3D Multifunctional Integumentary Membranes for Spatiotemporal Cardiac Measurements and Stimulation Across the Entire Epicardium. *Nat. Commun.* **2014**, *5*, 3329.
- (13) Fang, H.; Yu, K. J.; Gloschat, C.; Yang, Z. J.; Song, E. M.; Chiang, C. H.; Zhao, J. N.; Won, S. M.; Xu, S. Y.; Trumpis, M.; Zhong, Y. D.; Han, Z. J.; Xue, Y. G.; Xu, D.; Choi, S. W.; Cauwenberghs, G.; Kay, M.; Huang, Y. G.; Viventi, J.; Efimov, I. R.; Rogers, J. A. Capacitively Coupled Arrays of Multiplexed Flexible Silicon Transistors for Long-Term Cardiac Electrophysiology. *Nat. Biomed. Eng.* **2017**, *1*, No. 0038.
- (14) Fang, H.; Zhao, J. N.; Yu, K. J.; Song, E. M.; Farimani, A. B.; Chiang, C. H.; Jin, X.; Xue, Y. G.; Xu, D.; Du, W. B.; Seo, K. J.; Zhong, Y. D.; Yang, Z. J.; Won, S. M.; Fang, G. H.; Choi, S. W.; Chaudhuri, S.; Huang, Y. G.; Alam, M. A.; Viventi, J.; Aluru, N. R.; Rogers, J. A. Ultrathin, Transferred Layers of Thermally Grown Silicon Dioxide as Biofluid Barriers for Biointegrated Flexible Electronic Systems. *Proc. Natl. Acad. Sci. U. S. A.* **2016**, *113*, 11682–11687.
- (15) Viventi, J.; Kim, D. H.; Moss, J. D.; Kim, Y. S.; Blanco, J. A.; Annetta, N.; Hicks, A.; Xiao, J. L.; Huang, Y. G.; Callans, D. J.; Rogers, J. A.; Litt, B. A Conformal, Bio-Interfaced Class of Silicon Electronics for Mapping Cardiac Electrophysiology. *Sci. Transl. Med.* **2010**, *2*, 24ra22–24ra22.
- (16) Escabi, M. A.; Read, H. L.; Viventi, J.; Kim, D. H.; Higgins, N. C.; Storace, D. A.; Liu, A. S. K.; Gifford, A. M.; Burke, J. F.; Campisi, M.; Kim, Y. S.; Avrin, A. E.; Van der Spiegel, J.; Huang, Y. G.; Li, M.; Wu, J.; Rogers, J. A.; Litt, B.; Cohen, Y. E. A High-Density, High-Channel Count, Multiplexed μ ECOG Array for Auditory-Cortex Recordings. *J. Neurophysiol.* **2014**, *112*, 1566–1583.
- (17) Someya, T.; Kato, Y.; Sekitani, T.; Iba, S.; Noguchi, Y.; Murase, Y.; Kawaguchi, H.; Sakurai, T. Conformable, Flexible, Large-Area Networks of Pressure and Thermal Sensors with Organic Transistor Active Matrixes. *Proc. Natl. Acad. Sci. U. S. A.* **2005**, *102*, 12321–12325.
- (18) Lacour, S. P.; Jones, J.; Wagner, S.; Li, T.; Suo, Z. G. Stretchable Interconnects for Elastic Electronic Surfaces. *Proc. IEEE* **2005**, *93*, 1459–1467.
- (19) Tian, B. Z.; Cohen-Karni, T.; Qing, Q.; Duan, X. J.; Xie, P.; Lieber, C. M. Three-Dimensional, Flexible Nanoscale Field-Effect Transistors as Localized Bioprobes. *Science* **2010**, *329*, 830–834.
- (20) Takei, K.; Takahashi, T.; Ho, J. C.; Ko, H.; Gillies, A. G.; Leu, P. W.; Fearing, R. S.; Javey, A. Nanowire Active-Matrix Circuitry for Low-Voltage Macroscale Artificial Skin. *Nat. Mater.* **2010**, *9*, 821–826.
- (21) Schwartz, G.; Tee, B. C. K.; Mei, J. G.; Appleton, A. L.; Kim, D. H.; Wang, H. L.; Bao, Z. N. Flexible Polymer Transistors with High Pressure Sensitivity for Application in Electronic Skin and Health Monitoring. *Nat. Commun.* **2013**, *4*, 1859.
- (22) Wu, W. Z.; Wen, X. N.; Wang, Z. L. Taxel-Addressable Matrix of Vertical-Nanowire Piezotronic Transistors for Active and Adaptive Tactile Imaging. *Science* **2013**, *340*, 952–957.
- (23) Laks, M. M.; Arzbaecher, C. R.; Bailey, J. J.; Geselowitz, D. B.; Berson, A. S. Recommendations for Safe Current Limits for Electrocardiographs - A Statement for Healthcare Professionals from the Committee on Electrocardiography. *Circulation* **1996**, *93*, 837–839.
- (24) Swerdlow, C. D.; Olson, W. H.; O'Connor, M. E.; Gallik, D. M.; Malkin, R. A.; Laks, M. Cardiovascular Collapse Caused by Electrocardiographically Silent 60-Hz Intracardiac Leakage Current - Implications for Electrical Safety. *Circulation* **1999**, *99*, 2559–2564.
- (25) Bowman, L.; Meindl, J. D. The Packaging of Implantable Integrated Sensors. *IEEE Trans. Biomed. Eng.* **1986**, *33*, 248–255.
- (26) Bazaka, K.; Jacob, M. Implantable Devices: Issues and Challenges. *Electronics* **2013**, *2*, 1–34.
- (27) Fairfield, J. A. Nanostructured Materials for Neural Electrical Interfaces. *Adv. Funct. Mater.* **2018**, *28*, 1701145.
- (28) Li, J.; Song, E.; Chiang, C. H.; Yu, K. J.; Koo, J.; Du, H.; Zhong, Y.; Hill, M.; Wang, C.; Zhang, J.; Chen, Y.; Tian, L.; Zhong, Y.; Fang, G.; Viventi, J.; Rogers, J. A. Conductively Coupled Flexible Silicon Electronic Systems for Chronic Neural Electrophysiology. *Proc. Natl. Acad. Sci. U. S. A.* **2018**, *115*, E9542–E9549.
- (29) Lee, Y. K.; Yu, K. J.; Song, E. M.; Barati Farimani, A.; Vitale, F.; Xie, Z. Q.; Yoon, Y.; Kim, Y.; Richardson, A.; Luan, H. W.; Wu, Y. X.; Xie, X.; Lucas, T. H.; Crawford, K.; Mei, Y. F.; Feng, X.; Huang, Y. G.; Litt, B.; Aluru, N. R.; Yin, L.; Rogers, J. A. Dissolution of Monocrystalline Silicon Nanomembranes and Their Use as Encapsulation Layers and Electrical Interfaces in Water-Soluble Electronics. *ACS Nano* **2017**, *11*, 12562–12572.
- (30) Lee, Y. K.; Yu, K. J.; Kim, Y.; Yoon, Y.; Xie, Z. Q.; Song, E. M.; Luan, H. W.; Feng, X.; Huang, Y. G.; Rogers, J. A. Kinetics and Chemistry of Hydrolysis of Ultrathin, Thermally Grown Layers of Silicon Oxide as Biofluid Barriers in Flexible Electronic Systems. *ACS Appl. Mater. Interfaces* **2017**, *9*, 42633–42638.
- (31) Guldan, A.; Schiller, V.; Steffen, A.; Balk, P. Formation and Properties of TiSi_2 Films. *Thin Solid Films* **1983**, *100*, 1–7.
- (32) Herner, S. B.; Jones, K. S.; Gossmann, H. J.; Poate, J. M.; Luftman, H. S. Point Defects in Si after Formation of a TiSi_2 Film: Evidence for Vacancy Supersaturation and Interstitial Depletion. *Appl. Phys. Lett.* **1996**, *68*, 1687–1689.
- (33) Li, D. F.; Gu, C. Z.; Guo, C. X.; Yue, S. L.; Hu, C. W. Low Resistivity C54 phase TiSi_2 Films Synthesized by a Novel Two-Step Method. *Chin. Phys. Lett.* **2003**, *20*, 1329–1332.
- (34) Song, E. M.; Lee, Y. K.; Li, R.; Li, J. H.; Jin, X.; Yu, K. J.; Xie, Z. Q.; Fang, H.; Zhong, Y. D.; Du, H. N.; Zhang, J. Z.; Fang, G. H.; Kim, Y.; Yoon, Y.; Alam, M. A.; Mei, Y. F.; Huang, Y. G.; Rogers, J. A. Transferred, Ultrathin Oxide Bilayers as Biofluid Barriers for Flexible Electronic Implants. *Adv. Funct. Mater.* **2018**, *28*, 1702284.
- (35) Chang, J. K.; Emon, M. A. B.; Li, C. S.; Yang, Q. S.; Chang, H. P.; Yang, Z. J.; Wu, C. I.; Saif, M. T.; Rogers, J. A. Cytotoxicity and in Vitro Degradation Kinetics of Foundry-Compatible Semiconductor Nanomembranes and Electronic Microcomponents. *ACS Nano* **2018**, *12*, 9721–9732.
- (36) Kang, S. K.; Park, G.; Kim, K.; Hwang, S. W.; Cheng, H. Y.; Shin, J. H.; Chung, S. J.; Kim, M.; Yin, L.; Lee, J. C.; Lee, K. M.; Rogers, J. A. Dissolution Chemistry and Biocompatibility of Silicon- and Germanium-Based Semiconductors for Transient Electronics. *ACS Appl. Mater. Interfaces* **2015**, *7*, 9297–9305.
- (37) Trumbo, P.; Yates, A. A.; Schlicker, S.; Poos, M. Dietary Reference Intakes: Vitamin A, Vitamin K, Arsenic, Boron, Chromium, Copper, Iodine, Iron, Manganese, Molybdenum, Nickel, Silicon, Vanadium, and Zinc. *J. Am. Diet. Assoc.* **2001**, *101*, 294–301.
- (38) Danckwerts, P. V. Absorption by Simultaneous Diffusion and Chemical Reaction. *Trans. Faraday Soc.* **1950**, *46*, 300–304.
- (39) Cowan, K. G.; Harrison, J. A. The Dissolution of Magnesium in Cl⁻ and F⁻ Containing Aqueous Solutions. *Electrochim. Acta* **1979**, *24*, 301–308.
- (40) Taub, I. A.; Roberts, W.; LaGambina, S.; Kustin, K. Mechanism of Dihydrogen Formation in the Magnesium-Water Reaction. *J. Phys. Chem. A* **2002**, *106*, 8070–8078.
- (41) Li, R.; Cheng, H. T.; Su, Y. W.; Hwang, S. W.; Yin, L.; Tao, H.; Brenckle, M. A.; Kim, D. H.; Omenetto, F. G.; Rogers, J. A.; Huang, Y. G. An Analytical Model of Reactive Diffusion for Transient Electronics. *Adv. Funct. Mater.* **2013**, *23*, 3106–3114.
- (42) Yu, K. J.; Kuzum, D.; Hwang, S. W.; Kim, B. H.; Juul, H.; Kim, N. H.; Won, S. M.; Chiang, K.; Trumpis, M.; Richardson, A. G.; Cheng, H. Y.; Fang, H.; Thompson, M.; Bink, H.; Talos, D.; Seo, K. J.; Lee, H. N.; Kang, S. K.; Kim, J. H.; Lee, J. Y.; Huang, Y. G.; Jensen,

F. E.; Dichter, M. A.; Lucas, T. H.; Viventi, J.; Litt, B.; Rogers, J. A. Bioresorbable Silicon Electronics for Transient Spatiotemporal Mapping of Electrical Activity from the Cerebral Cortex. *Nat. Mater.* **2016**, *15*, 782–791.

(43) Yin, L.; Cheng, H. Y.; Mao, S. M.; Haasch, R.; Liu, Y. H.; Xie, X.; Hwang, S. W.; Jain, H.; Kang, S. K.; Su, Y. W.; Li, R.; Huang, Y. G.; Rogers, J. A. Dissolvable Metals for Transient Electronics. *Adv. Funct. Mater.* **2014**, *24*, 645–658.